npj computational materials

www.nature.com/npjcompumats

ARTICLE OPEN

Check for updates

High-throughput first-principle prediction of collinear magnetic topological materials

Yunlong Su[1], Jiayu Hu[1], Xiaochan Cai[1], Wujun Shi[2,3], Yunyouyou Xia[1,4], Yuanfeng Xu[5,6], Xuguang Xu[1], Yulin Chen[1,4,7] and Gang Li[1,4]✉

The success of topological band theory and symmetry-based topological classification significantly advances our understanding of the Berry phase. Based on the critical concept of topological obstruction, efficient theoretical frameworks, including topological quantum chemistry and symmetry indicator theory, were developed, making a massive characterization of real materials possible. However, the classification of magnetic materials often involves the complexity of their unknown magnetic structures, which are often hard to know from experiments, thus, hindering the topological classification. In this paper, we design a high-throughput workflow to classify magnetic topological materials by automating the search for collinear magnetic structures and the characterization of their topological natures. We computed 1049 chosen transition-metal compounds (TMCs) without oxygen and identified 64 topological insulators and 53 semimetals, which become 73 and 26 when U correction is further considered. Due to the lack of magnetic structure information from experiments, our high-throughput predictions provide insightful reference results and make the step toward a complete diagnosis of magnetic topological materials.

npj Computational Materials (2022)8:261 ; https://doi.org/10.1038/s41524-022-00954-w

INTRODUCTION

Beyond the Landau symmetry-breaking paradigm, the discovery of topological states of matter further extends our fundamental understanding of wave function and its phase evolution in parameter space. The attribution of the quantized Hall conductance to an integer number of Thouless-Kohomoto-Nightingale-Nijs (TKNN)[1,2] opens the avenue for topological classification of electronic wave functions in terms of topological invariant. Quantum anomalous Hall effect[3], quantum spin Hall effect[4–6], three-dimensional topological insulators[7,7–11], topological crystalline insulators[12], Weyl semimetals[13–17], nodal line semimetals[18–23] triple fermions[24–31], six-fold[32–38], eight-fold fermions[39–41], Dirac semimetals[42–54], and magnetic topological insulators[55–74], etc., were soon theoretical proposed and experimentally discovered, which are characterized by different topological numbers, by which topological phases differ each other. Except for the Chern insulator and Weyl semimetals, all other topological states are protected by crystalline and time-reversal (TR) symmetry. Group theory plays an essential role in classifying topological states.

Utilizing group theory, band degeneracy and connectivity at/between different maximal **K**-points can be precisely determined, which lays the theoretical basis for automating the topological classification of real material. Before the comprehensive understanding of the relationship between topological invariant and group symmetry, there already exists a simplified algorithm that can quickly diagnose the three-dimensional (3D) topological insulators with inversion symmetry[75]. At each time-reversal invariant momentum (TRIM), Bloch wave functions carry definite eigenvalues of the inversion operator. The topological invariant of 3D TIs can be calculated as the product of parity eigenvalues of all occupied bands at all eight TRIM. The connection of topological invariant to the discrete crystalline symmetry eigenvalues at a finite number of TRIM greatly simplifies the classification of topological materials, as tedious integration of wave functions in the Brillouin zone (BZ) is no more required.

The Fu-Kane scheme for topological invariant for inversion invariant systems greatly inspires the search for quick diagnosis schemes for systems with other symmetries. There are two closely related schemes proposed simultaneously in 2017, i.e., topological quantum chemistry (TQC)[76] and symmetry indicator (SI) theory[77,78], which are highly efficient in diagnosing nearly all known topological phases. Consequently, high-throughput characterization of inorganic materials was quickly carried out with astonishing accuracy and efficiency[79]. Most nonmagnetic stable materials tabulated in ICSD (Inorganic Crystal Structure Database) and *Materials Project* have been examined and topologically classified, representing a great success of the TQC and SI theories[76–78].

The same idea has also been extended to the magnetic space group ($\mathcal{MSG}$)[80,81]. With the carefully designed computer tools, 549 magnetic materials from *MAGNDATA* database were first topologically classified by Benevig's group[82], and several attractive magnetic topological material candidates were discovered. However, unlike the classification of nonmagnetic materials, large-scale diagnosis of magnetic materials is further subject to the uncertainty of the magnetic configurations. Experimental techniques for magnetic structures are available only for high-quality single crystals, and the determination of a magnetic structure usually requires much more effort than just characterizing a crystal structure. For this reason, *MAGNDATA* only contains the magnetic configurations of a tiny portion of magnetic materials. Magnetic structures of many more materials are not yet available experimentally. Thus, although the

[1]School of Physical Science and Technology, ShanghaiTech University, 201210 Shanghai, China. [2]Center for Transformative Science, ShanghaiTech University, 201210 Shanghai, China. [3]Shanghai High Repetition Rate XFEL and Extreme Light Facility (SHINE), ShanghaiTech University, 201210 Shanghai, China. [4]ShanghaiTech Laboratory for Topological Physics, ShanghaiTech University, 201210 Shanghai, China. [5]Center for Correlated Matter and School of Physics, Zhejiang University, 310058, Hangzhou, China. [6]Department of Physics, Princeton University, Princeton, NJ, USA. [7]Department of Physics, Clarendon Laboratory, University of Oxford, Parks Road, Oxford OX1 3PU, UK.
✉email: ligang@shanghaitech.edu.cn

theoretical foundation and the right computer tools have been developed, massive magnetic-material diagnosis is apparently hindered by the lack of knowledge of magnetic structures.

Without experimental insights, to make progress on the high-throughput topological diagnosis of magnetic materials, theoretically, we have to first predict a candidate magnetic structure before topological characterization. Determining magnetic configuration is a highly nontrivial task, and one can only locate the magnetic ground state within the space of a limited number of initial configurations. The reliability of such theoretical prediction highly depends on the available initial configurations. In this work, we restrict ourselves to the collinear magnetic structures to feature a high-throughput calculation. We design a workflow to examine the possible collinear magnetic structures theoretically and, subsequently, determine their topological natures. Because of the theoretical nature of the proposed magnetic structures, our diagnosis no longer provides a definite answer to the topological nature of the examined magnetic materials. It only offers a possible candidate topological characterization, which awaits further experimental verification. Nevertheless, our work screens the search area and provides valuable insights into future experimental exploration. Several interesting magnetic topological materials have been proposed, making a first step toward the complete diagnosis of magnetic topological materials.

RESULTS

Design of workflow

To facilitate a high-throughput prediction of magnetic topological materials, we design a workflow by combining two efficient high-throughput algorithms to examine possible collinear magnetic structures of transition-metal (TM) compounds and characterize their topological nature. The workflow is designed for FireWork by utilizing atomate[83]. In this paper, we concentrate on the TM binary and ternary compounds with strong spin-orbit coupling (SOC). Our choice of TM binary compounds consists of magnetic elements including V, Cr, Mn, Co, Fe, Ni, Ru, Mo, and Cu, and elements with strong SOC including Tl, Pb, Bi, In, Sn, Sb, Te, Ga, Ge, As, Se, Al, Si, P, and S. Alkali metals including Li, Be, Na, Mg, K, Ca, Sr, Cs, and Ba are further included in ternary compounds. We restrict the total atom numbers in a primitive cell to be less than 20 to facilitate a fast diagnosis. In total, we filtered 1049 TM compounds (TMCs) from *Materials Project* as our initial database to demonstrate the power of our scheme. The above choice of magnetic materials is only for demonstration purposes. Our workflow is ready to apply to any magnetic material and predict its collinear magnetic state with topological classification.

We show the workflow in Fig. 1, which consists of three major steps. In the first and the third steps, we adopt open-source implementations[82,84], which we will also briefly discuss in the Methods section. We design the second step to synergy the two established workflows simultaneously.

In step 1, we use the high-throughput framework[84] developed by M. K. Horton et al. in 2019 to search the candidate collinear magnetic ground state of a given crystal. The proposed searching algorithm has been tested over 64 collinear antiferromagnetic materials in *MAGNDATA* and obtained 60% correct predictions as compared to the experimental magnetic orderings[84]. Based on this workflow, collinear magnetic orderings of more than 3000 transition-metal oxides were examined[85], displaying a high efficiency in the theoretical screening of magnetic topological materials. We note that our workflow distinguishes from the work of Frey et al. [85] in two aspects. First, the magnetic materials we examined do not contain oxygen but elements with strong SOC to favor nontrivial topology and, at the same time, to favor possibly an easy experimental preparation. Second, we did not restrict the materials to be inversion symmetric as we further automate the

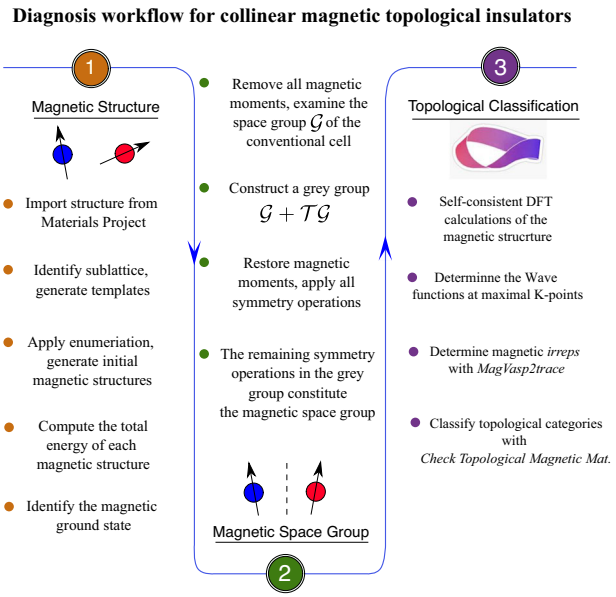

Fig. 1 Diagnosis workflow for high-throughput prediction of collinear magnetic topological materials. The workflow consists of three major steps: (1) Identification of collinear magnetic structure. (2) Determination of the corresponding magnetic space group. (3) Classification of the topological categories with TQC.

topological classification with TQC algorithm[76,82], which is a universal algorithm applicable to materials both with and without inversion symmetry. In step 2, we identify the $\mathcal{MSG}$ of the obtained magnetic structures in step 1. The knowledge of the magnetic space group is crucial to the third step, which works with the maximal **K**-points and the character table of a given $\mathcal{MSG}$. In the last step, we employed the magnetic TQC routine *MagVasp2trace* and *Check Topological Magnetic Mat*. module from Bilbao Crystalline Server (BCS) to examine the irreducible representations (*irreps*) and, finally, the topological classification. We refer to the details of the collinear magnetic structure search and the magnetic TQC to their original works[76,82,84]. We also provide a short explanation in Supplementary Methods.

The essential step to connecting the two algorithms in steps 1 and 3 is to efficiently identify the magnetic space group of any given magnetic material. To this end, we design a function based on *spglib*[86] which quickly finds all symmetry operations based on the paramagnetic group. We define the paramagnetic group as the symmetry group for the same magnetic unit cell but without local moments. After removing all magnetic moments, the unit cell can be a conventional one. We keep the unit cell size and all atomic positions unchanged and determine the space group of it, which we denote as $\mathcal{G}$. If the paramagnetic unit cell is a conventional one, $\mathcal{G}$ contains fractional lattice translations, with the translational vector being the unit vectors of its primitive cell. We further construct of a gray group of $\mathcal{G}$ denoted as $\mathcal{G}_g = \mathcal{G} + \mathcal{T}\mathcal{G}$. $\mathcal{G}_g$ contains both unitary and anti-unitary operations, and it includes all the operations of the desired magnetic space group. However, $\mathcal{G}_g$ also contains many redundant operations with respect to the magnetic unit cell, which we will remove by applying all operations in this grep group to the magnetic cell and testing their applicability. All operations passing the symmetry check for the magnetic unit cell constitute the $\mathcal{MSG}$. Comparing these symmetries with those listed in *MGENPOS* of BCS, we obtain the correct $\mathcal{MSG}$ in BNS notation[87]. At the same time, we transform the magnetic unit cell to the same convention (standard magnetic primitive) of BCS as required by the topological characterization module.

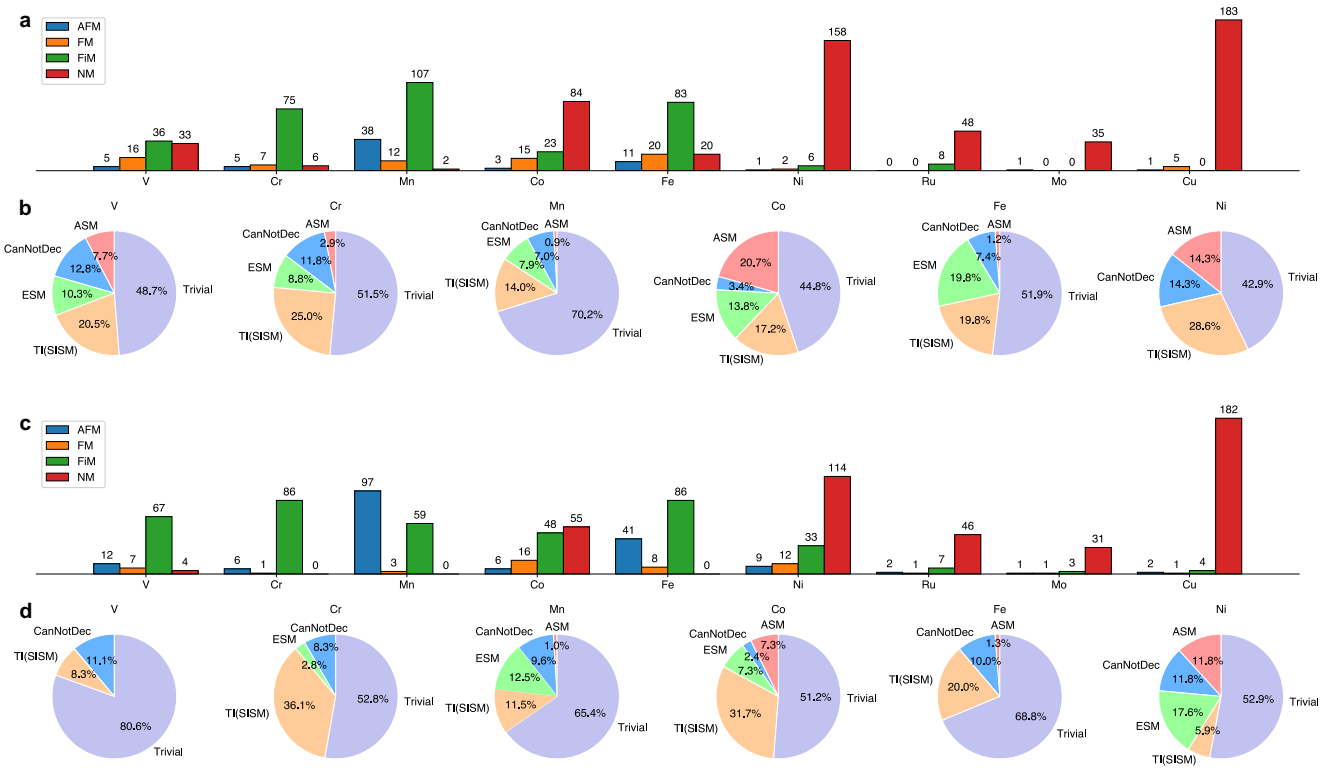

Fig. 2 Summary of magnetic and topological diagnosis of 1049 TMCs. Panels **a**, **b** correspond to the calculations without U. In **a**, each column chart shows the statistic of magnetic ground states theoretically predicted by the workflow. Except for Ni, Ru, Mo, and Cu compounds which have dominant nonmagnetic ground states, the ground states of the other compounds display certain magnetic ordering. In **b**, all materials with predicted magnetic ground states are further examined by topological characterization. Trivial materials and materials that cannot be successfully classified are over 50%. Our workflow identifies two categories of magnetic materials: TI(SISM) and semimetals (ESM/ASM). See the main text for their definitions. Panels **c**, **d** are the same as **a**, **b** but with U corrections.

Statistics

Figure 2 summarizes the high-throughput screening of magnetic topological materials from our workflow. We diagnosed 1049 chosen TMCs in two runs, one with spin-polarized DFT calculations and the other with spin-polarized DFT+U calculations with the U parameters[88] for each transition-metal element specified in the Supplementary Methods. The first two rows (a, b) summarize the diagnosis without U correction, and (c, d) correspond to calculations with U. We show the statistical summary of the collinear magnetic structure search in (a, c) and the topological characterization in (b, d) for the screened magnetic materials from the first step. The four columns labeled in blue, yellow, green, and red in (a, c) correspond to the number of materials identified as antiferromagnetic (AFM), ferromagnetic (FM), ferrimagnetic (FiM), and nonmagnetic (NM), respectively. The majority of compounds consisting of Ni, Ru, Mo, and Cu are nonmagnetic and are not passed to the topological characterization. We only tried with materials showing magnetic ground states.

In (b, d) of Fig. 2, we show the topological classification with the complete list of magnetic TI and magnetic SM given in Supplementary Table 1. Promisingly, a large portion of the magnetic materials predicted in the first step, i.e., magnetic structure search, is found to carry certain nontrivial topology. In calculations with U correction, the portion of nontrivial materials becomes less. For the various magnetic topological phases with nonzero invariants, we categorize them mainly into two classes. One contains systems with stable topological indices. According to refs. [76,82], it includes stable magnetic topological insulators and Smith-index semimetal (SISM). The latter are semimetals with unavoidable level crossings at generic points. The second class contains semimetals with band crossings at high-symmetry points, lines, or planes in the BZ. The band crossings of these semimetals can be either symmetry enforced, which we further term as symmetry-enforced semimetal (ESM), or the semimetals with accidental band crossings (ASM). The relative ratio of two topological class materials, i.e., TI/SISM and semimetals (ESM, ASM), is shown in (b, d) of Fig. 2. There are also materials with a magnetic ground state that cannot be topologically classified. This is due to either the poor convergence of self-consistent DFT calculation with SOC or the low symmetry of the wave functions. The irreps decomposition cannot be accomplished for the given magnetic space group.

A rough comparison of the two runs indicates that the inclusion of U corrections tends to stabilize magnetic ground states but breaks the nontrivial topology. The number of materials with certain magnetic ordering increases, but the number of TI(SISM) and ESM/ASM becomes less. Without U correction, we discovered 68 magnetic TI/SISM and 53 SMs. In the second run with U correction, these numbers become 73 and 26, respectively. We note that the calculations depend on the choices of U parameters and the trend may not lead to a general conclusion.

In the following, we take a closer look at three representative materials, i.e., SrMnSn, $Rb(CrS_2)_2$, and $Cs(MnP)_2$. Single crystals of SrMnSn and $Cs(MnP)_2$ are available in experiments[89,90]. SrMnSn is a G-type AFM with the magnetic unit cell doubled along the *c*-axis forming a tetragonal lattice. $Cs(MnP)_2$ is isotopic with $BaZn_2P_2$. It is paramagnetic following the Curie-Weiss law above 110 K, below which it becomes antiferromagnetic[90]. According to Table SI-2 to Table SI-5, the three material examples belong to ESM, SISM, and axion insulator, respectively. $Rb(CrS_2)_2$ is ferrimagnetic, with magnetic moment mainly from chromium atoms. Negligibly small magnetic moments exist at sulfur sites. We ignored them in the DFT self-consistent and band structure calculations. $Cs(MnP)_2$ is

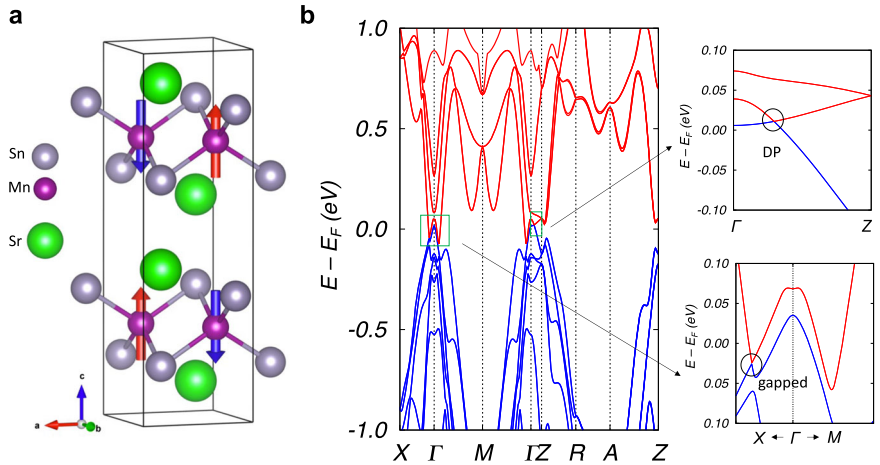

Fig. 3 Magnetic Dirac nodal loop semimetal mp-20759 SrMnSn. a Crystal and AFM structure of SrMnSn. **b** The electronic structure of SrMnSn displays a symmetry-protected Dirac point along Γ-Z, and a symmetry-enforced Dirac nodal loop along R-A-Z.

antiferromagnetic with either G-type or A-type depending on the values of U.

Representative ESM material: SrMnSn. In our diagnosis, SrMnSn is identified as a trivial semiconductor in DFT calculations but a symmetry-enforced semimetal in DFT + U calculations. In the following, we focus on the DFT + U results and examine the symmetry protection in more detail. SrMnSn belongs to $\mathcal{MSG}$ 138.528 (P_c4_2/ncm), which contains both inversion symmetry and $S = \mathcal{T}\tau_{z/2}$. Similar to $MnBi_2Te_4$, $S^2 = -e^{-ik_z}$ takes two values ± 1 depending on $k_z = 0/\pi$. Thus, S behaves as an effective time-reversal symmetry at $k_z = 0$ plane, where a Z_2 topological invariant can be defined. Moreover, in SrMnSn, due to the simultaneous presence of inversion symmetry $\mathcal{P}$, one can further define a joint operation $S' = \mathcal{PT}\tau_{z/2}$, which is anti-unitary and squares to -1. Under the protection of S', despite the loss of time-reversal symmetry, SrMnSn still has Kramer's degeneracy as in a nonmagnetic system. Every Bloch band in Fig. 3b is at least two-fold degenerate.

In SrMnSn, the highest valence and the lowest conduction band cross at the Fermi level, forming a magnetic Dirac point. The antiferromagnetic Dirac semimetal has been reported in orthorhombic CuMnAs[91], in which inversion symmetry is broken but the joint operation of $\mathcal{PT}$ is preserved, protecting its Kramer's degeneracy. In contrast, SrMnSn is inversion symmetric but $\mathcal{PT}$ is broken. The Kramer's degeneracy in SrMnSn is protected by the product of $\mathcal{PT}$ and the half-lattice translation $\tau_{z/2}$, i.e., S' defined above. In SrMnSn, the magnetic Dirac point along $\Gamma - Z$ is protected by S' and a four-fold skew rotation. Such protection mechanism is a magnetic analog of the rotational-symmetry-protected Dirac point in nonmagnetic systems[92].

Furthermore, in SrMnSn, there is also symmetry-enforced 4-fold band degeneracies at X, M, Z. More interestingly, bands along high-symmetry lines R-A-Z form magnetic nodal loops, common in nonmagnetic systems but rarely reported in magnetic materials. The symmetry protections of X, M, Z, and R-A-Z are similar; here we take X as an illustration.

At X, the magnetic little co-group is $mmm1'$ containing two orthogonal skew rotations. All Bloch bands can be further labeled by their eigenvalues. Let's take the unitary glide mirror reflection $\hat{g}_x : (-x + 1/2, y, z + 1/2) \otimes (-i\sigma_x)$ as an example. The two separated operations of $\hat{g}_x$ act on the coordinate and spin spaces, respectively. We neglect the irrelevant operation on local moments for simplicity. There is also $\hat{g}_y = (x, -y + 1/2, z + 1/2) \otimes (-i\sigma_y)$, which anticommutes with $\hat{g}_x$, i.e., $\{\hat{g}_x, \hat{g}_y\} = 0$. At X, Bloch state is an eigenstate of $\hat{g}_y$ with $\hat{g}_y|\psi\rangle = \pm i|\psi\rangle$. It is easy to prove that $S'|\psi\rangle$ has the same $\hat{g}_y$ eigenvalue as $|\psi\rangle$. While, $\hat{g}_x|\psi\rangle$ and $S'\hat{g}_x|\psi\rangle$ have opposite eigenvalues of $|\psi\rangle$ under $\hat{g}_y$. Thus, four states $(|\psi\rangle, S'|\psi\rangle)$ and $(\hat{g}_x|\psi\rangle, S'\hat{g}_x|\psi\rangle)$ stay degenerate at X, forming a stable four-fold band crossing point. A similar analysis shows that along R-A, $\hat{g}_y$ and $\hat{g}_z := (x + 1/2, y + 1/2, -z) \otimes (-i\sigma_z)$ anticommute and enforces a four-fold nodal line structure. Along $A - Z$, the symmetries protecting the four-fold magnetic nodal line are $\hat{c}_{2xy} : (y + 1/2, x + 1/2, -z) \otimes -i\sqrt{2}/2(\sigma_x + \sigma_y)$ and $\hat{g}_{xy} : (y, x, z) \otimes i\sqrt{2}/2(\sigma_x - \sigma_y)$.

Our high-throughput calculations correctly predict SrMnSn to be magnetic ESM. Further analysis indicates the coexistence of multiple nodal structures in this system. The presence of Kramer's degeneracy, the magnetic Dirac point, and four-fold magnetic nodal lines make SrMnSn an appealing material platform for experiments to study magnetic ESM with multiple nodal structures.

Representative SISM material: $Rb(CrS_2)_2$. According to the automated topological characterization in Supplementary Tables 2 and 3, $Rb(CrS_2)_2$ is a TI/SISM with stable topological invariant $\eta_{4l}z_{2l,1}z_{2l,2} = [300]/[100]$ in calculations without/with U, respectively. $\eta_{4l} = 1, 3$ belong to the same topological class, both indicating a Weyl semimetal with odd pairs of Weyl nodes in the BZ[76,82].

$\mathcal{MSG}$ of $Rb(CrS_2)_2$ is 15.89, containing inversion symmetry but no pure fractional lattice translation. Although in $Rb(CrS_2)_2$ one cannot globally define an effective time-reversal symmetry as in SrMnSn, a local definition is still possible. $\mathcal{MSG}$ 15.89 contains two anti-unitary operations. Given the inversion symmetry, all k-points that respect these anti-unitary symmetries will have a Kramer's pair to degenerate in energy. We observe a double band degeneracy at M_1 and a two-fold nodal line along $S - R_2$, as shown in Fig. 4b.

The valence and conduction bands of $Rb(CrS_2)_2$ separate along the k-path in Fig. 4b. The Fermi surface consists mainly of the Cr-d orbitals. Due to the small SOC, the energy separation between the valence and the conduction bands is small. When the SOC is turned off, $Rb(CrS_2)_2$ becomes an SM with a nodal ring formed by the crossing of the conduction and the valence bands, which are gapped into Weyl SM with discrete Weyl nodes when SOC is included. Due to the inversion symmetry, each pair of Weyl nodes appear at the same binding energy and locate precisely at the opposite momenta. All Weyl nodes around the Fermi level have a chiral charge of ±1. The helicoid surface states connecting two nodes with opposite chirality form the Fermi arc shown in Fig. 4c, d. We observed Fermi arcs states on both (001) and (100) surfaces. On the right plot in (c), we also project four pairs of Weyl nodes to the (001) surface. It is clear that these Weyl nodes are the sources and sinks of the Fermi arcs.

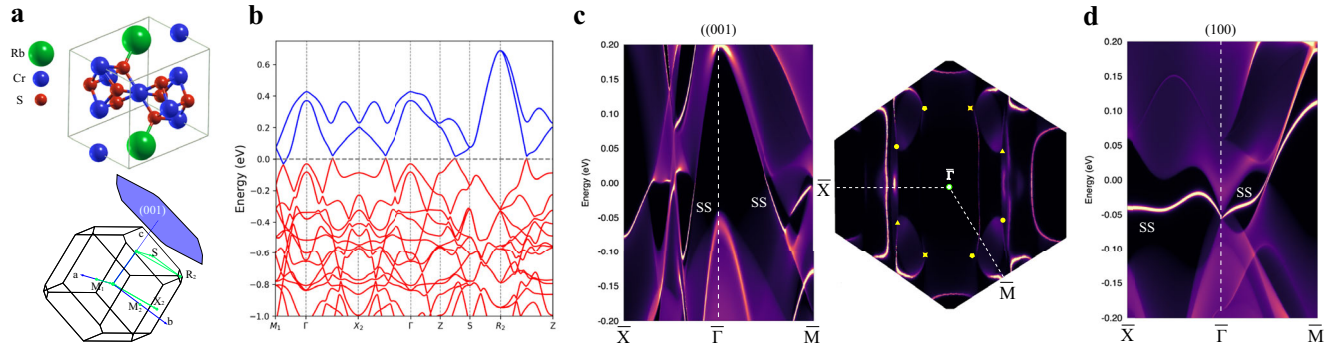

Fig. 4 Smith-index semimetals mp-1238796 $Rb(CrS_2)_2$ with stable invariant $\eta_{4l} = 3$. a The crystal structure and Brillouin zone. **b** The electronic structure with SOC. The red and blue colors denote the occupied and unoccupied bands, respectively. Panels **c** and **d** show the surface states at (001) and (100) surfaces. $Rb(CrS_2)_2$ contains four pairs of Weyl points around the Fermi level within the energy range of ±0.015 eV, which are marked as yellow dots in the $E = E_F$ constant energy plot in **c**. Two Weyl nodes with the same shape are related by inversion symmetry and reside at the same binding energy.

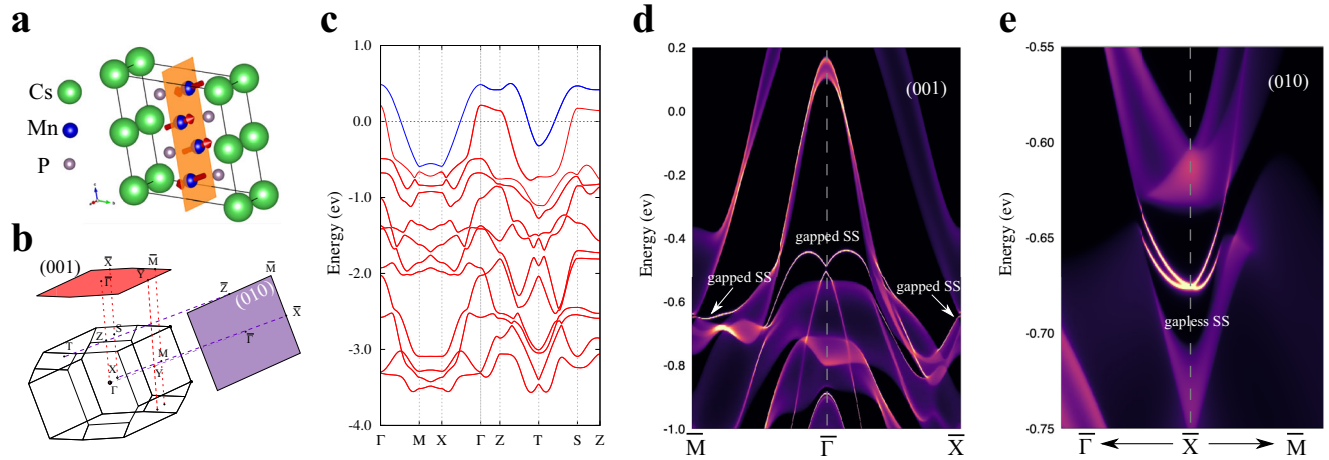

Fig. 5 Axion insulator mp-11181 $Cs(MnP)_2$ with stable invariant $\eta_{4l} = 2$. a The crystal structure and **b** Brillouin zone. **c** The electronic structure with SOC. The red and blue colors denote the occupied and unoccupied bands, respectively. Panels **d** and **e** show the surface states at (001) and (010) surfaces, with the surface BZ shown in **b**. Due to the different net surface magnetism, we observed the gap and the gapless surface states at (001) and (010), respectively.

Representative axion material: $Cs(MnP)_2$. $Cs(MnP)_2$ is theoretically predicted as an AFM insulator in both Supplementary Tables 2 and 3 consistent with the experimental report[90]. In both calculations, it is characterized as an axion insulator. The overall antiferromagnetic nature of the ground state agrees well with the experimental observation[90,93]. We note that we obtained two different AFM ground-state configurations depending on the values of U. Similar controversy also exists in experiments concerning the magnetic transition temperature and the ground-state order. Here we focus on the A-type AFM structure proposed in spin-polarized DFT + U calculations, in which the magnetic moments point to [-110] and antiferromagnetically align [010]. Due to the simultaneous presence of time-reversal and inversion symmetry in $Cs(MnP)_2$, every band is doubly degenerate as in nonmagnetic systems. The electronic structure shows a metallic behavior with both the lowest conduction band and the top valence band crossing the Fermi level. They overlap in energy but have no level crossings. Thus, a momentum-dependent chemical potential can separate them adiabatically, leading to a semiconductor.

We calculated the surface states at (001) surface, where time-reversal symmetry is broken. The net surface magnetism is finite. The surface states show a typical gapped structure. While on the (010) surface, where half-lattice translation along [001] and time-reversal define an effective surface time-reversal symmetry. Consequently, the surface states at (010) are gapless, as shown in Fig. 5e. This is a typical feature of magnetic topological insulators in which topological surface states display gaped/gapless structures at surface breaking/respecting time-reversal symmetry. The same behavior of topological surface states in $MnBi_2T_4$[62,74,94] and the calculated topological invariant $\eta_{4l} = 2$ confirm the A-type AFM $Cs(MnP)_2$ as an axion insulator.

DISCUSSIONS

In this paper, we presented an automated workflow to explore magnetic topological materials from the first principle. We combined two high-throughput algorithms to theoretically search collinear magnetic ground states and examined their topological nature. The first step of the workflow is to search the collinear magnetic ground state, which is accomplished by the algorithm proposed in ref. [84]. The subsequent topological characterization is done via the magnetic TQC theory[76,82]. We synchronized the two high-throughput workflows by efficiently determining the $\mathcal{MSG}$, refining the standard crystal structure, and interacting with the Bilbao crystallographic server.

To demonstrate the power and feasibility of the designed workflow, we examined 1049 binary and ternary compounds containing V, Cr, Mn, Co, Fe, Ni, Ru, Mo, and Cu. We did two runs of

calculations, i.e., one with U correction and the other without. Both runs predicted a considerably large number of collinear topological material candidates. Our high-throughput calculations predict highly relevant collinear topological material candidates and provide insightful guidance to further experimental investigations.

As the workflow only explores the collinear magnetic configurations, the readers need caution to understand our diagnosis results. The prediction presented in our work only offers a possible candidate topological characterization, which needs to be verified and corrected once the experimental magnetic structure is available. Our work provides a step toward a complete theoretical characterization of magnetic topological materials. Further improvement and optimization of the workflow are possible. (1) To accelerate the theoretical search, we have restricted the magnetic ground-state exploration in the non-relativistic case. The magnetic anisotropy was not taken into account. We include the SOC effect in step (3) and fix the magnetic moment to the *z*-direction of the standard conventional cell. The magnetic anisotropy energy (MAE) may be large in some materials such that their magnetic moments strongly prefer a specific direction. A high-throughput algorithm for determining MAE is desirable to get the moment orientation. (2) The current workflow only generates collinear magnetic configurations. Lattices of kagome, pyrochlore, etc., frustrated structures favoring noncollinear magnetic couplings, and interesting band topology cannot be correctly described by the current workflow. There is a strong demand to develop a workflow capable of efficiently exploring noncollinear magnetic structures. (3) We chose the initial ternary materials as the ones with TM elements, alkali atoms, and semiconductor elements of large SOC. However, most magnetic materials have relatively weak $d-p$ hybridization, such that the SOC gap is too small to facilitate an excellent insulating behavior. Diagnosing materials with strong SOC and strong $d-p$ hybridizations may lead to the discovery of excellent magnetic topological materials with both spin polarization and a large topological gap at the Fermi level. (4) In our DFT + U calculations, we chose the U parameter from first-principle estimation[88]. The resulting magnetic ordering and topological characterization, thus, depend on the U values. An unbias first-principle calculation without adjusting parameters, such as SCAN functional[95], can eliminate the uncertainty induced by the DFT + U functional.

METHOD

Our first-principle calculations are based on the generalized-gradient approximation (GGA) in the Perdew-Burke-Ernzerhof (PBE) form[96–100] within the framework of the density-functional theory (DFT) using projector-augmented-wave (PAW)[101] wave functions as implemented in the Vienna Ab-Initio Simulation Package (VASP)[102,103]. The cut-off energy for the wave functions was set at 500 eV. We performed two sets of calculations for comparison, i.e., one with spin-polarized DFT and the other one with spin-polarized DFT + U. In the latter, we took the ab-initio Hubbard correction parameters for V (3.909 eV), Cr (2.982 eV), Mn (4.710 eV), Co (5.237 eV), Fe (4.545 eV), Ni (5.847 eV), Cu (7.59 eV), Ru (2.972 eV), and Mo (2.431 eV) as suggested in ref. [88]. Fixed reciprocal space density was used for the Brillouin zone (BZ) sampling with $(k_1, k_2, k_3) = mul \times (1/a, 1/b, 1/c)$, where $mul = (NVabc)^{1/3}$. V is the volume of the reciprocal cell. N is the grid density per reciprocal cell (in the unit of $Å^{-3}$). N takes two different values, i.e., 64 in structure relaxation calculations and 100 in the charge self-consistent calculations. The self-consistent convergence threshold for total energy was set at 10^{-5} eV. During the magnetic structure search, we turned off the SOC to accelerate the calculations, which was included in the topological analysis. With SOC, the local frame of the magnetic moment becomes essential for systems with strong magnetic anisotropy. In our high-throughput calculations, the magnetic moments are aligned to the *z*-direction of the magnetic cell by default (see the Data availability section for the *mcif* files.). The magnetic moments will be further rotated to a new direction after transforming the magnetic cell to the standard primitive cell required by *MVasp2trace* and BCS. Finally, the edge states were calculated by using our in-house code *LTM* (L ibrary for T opological M aterial calculations) with the iterative Green's function approach[104] based on the maximally localized Wannier functions[105] obtained through the VASP2WANNIER90[106]. The chirality of Weyl nodes in mp-1238796 $Rb(CrS_2)_2$ was evaluated by using the WannierTools pacakge[107].

DATA AVAILABILITY

All data are available from the corresponding author upon reasonable request. The magnetic structures files and trace files generated by Mvasp2trace and band structures are available at https://github.com/GangLi_SHT/Collinear_MTQC.

CODE AVAILABILITY

The codes for steps 1 and 3 of the workflow are open-source and free of charge except for the VASP. The codes for automatic analysis of the magnetic space group are available at https://github.com/GangLi_SHT/Collinear_MTQC.

Received: 15 May 2022; Accepted: 13 December 2022;
Published online: 27 December 2022

REFERENCES

1. Klitzing, K. V., Dorda, G. & Pepper, M. New method for high-accuracy determination of the fine-structure constant based on quantized Hall resistance. *Phys. Rev. Lett.* **45**, 494 (1980).
2. Thouless, D. J., Kohmoto, M., Nightingale, M. P. & den Nijs, M. Quantized Hall conductance in a two-dimensional periodic potential. *Phys. Rev. Lett.* **49**, 405 (1982).
3. Haldane, F. D. M. Model for a quantum Hall effect without Landau levels: condensed-matter realization of the" parity anomaly". *Phys. Rev. Lett.* **61**, 2015 (1988).
4. Kane, C. L. & Mele, E. J. Z_2 topological order and the quantum spin Hall effect. *Phys. Rev. Lett.* **95**, 146802 (2005).
5. Bernevig, B. A., Hughes, T. L. & Zhang, S.-C. Quantum spin Hall effect and topological phase transition in HgTe quantum wells. *Science* **314**, 1757–1761 (2006).
6. König, M. et al. Quantum spin Hall insulator state in HgTe quantum wells. *Science* **318**, 766–770 (2007).
7. Fu, L., Kane, C. L. & Mele, E. J. Topological insulators in three dimensions. *Phys. Rev. Lett.* **98**, 106803 (2007).
8. Zhang, H. et al. Topological insulators in Bi_2Se_3, Bi_2Te_3 and Sb_2Te_3 with a single Dirac cone on the surface. *Nat. Phys.* **5**, 438–442 (2009).
9. Chen, Y. L. et al. Experimental realization of a three-dimensional topological insulator, Bi_2Te_3. *Science* **325**, 178–181 (2009).
10. Analytis, J. G. et al. Bulk Fermi surface coexistence with Dirac surface state in Bi_2Se_3: a comparison of photoemission and Shubnikov–de Haas measurements. *Phys. Rev. B* **81**, 205407 (2010).
11. Zhang, Y. et al. Crossover of the three-dimensional topological insulator Bi_2Se_3 to the two-dimensional limit. *Nat. Phys.* **6**, 584–588 (2010).
12. Fu, L. Topological crystalline insulators. *Phys. Rev. Lett.* **106**, 106802 (2011).
13. Wan, X., Turner, A. M., Vishwanath, A. & Savrasov, S. Y. Topological semimetal and Fermi-arc surface states in the electronic structure of pyrochlore iridates. *Phys. Rev. B* **83**, 205101 (2011).
14. Weng, H., Fang, C., Fang, Z., Bernevig, B. A. & Dai, X. Weyl semimetal phase in noncentrosymmetric transition-metal monophosphides. *Phys. Rev. X* **5**, 011029 (2015).
15. Huang, S.-M. et al. A Weyl Fermion semimetal with surface Fermi arcs in the transition metal monopnictide TaAs class. *Nat. Commun.* **6**, 7373 (2015).
16. Lv, B. Q. et al. Experimental discovery of Weyl semimetal TaAs. *Phys. Rev. X* **5**, 031013 (2015).
17. Yang, L. X. et al. Weyl semimetal phase in the non-centrosymmetric compound TaAs. *Nat. Phys.* **11**, 728–732 (2015).
18. Yang, B.-J., Bojesen, T. A., Morimoto, T. & Furusaki, A. Topological semimetals protected by off-centered symmetries in nonsymmorphic crystals. *Phys. Rev. B* **95**, 075135 (2017).
19. Mullen, K., Uchoa, B. & Glatzhofer, D. T. Line of Dirac nodes in hyperhoneycomb lattices. *Phys. Rev. Lett.* **115**, 026403 (2015).

20. Chan, Y.-H., Chiu, C.-K., Chou, M. Y. & Schnyder, A. P. Ca_3P_2 and other topological semimetals with line nodes and drumhead surface states. *Phys. Rev. B* **93**, 205132 (2016).
21. Yu, R., Weng, H., Fang, Z., Dai, X. & Hu, X. Topological node-line semimetal and Dirac semimetal state in antiperovskite Cu_3PdN. *Phys. Rev. Lett.* **115**, 036807 (2015).
22. Li, S. et al. Almost ideal nodal-loop semimetal in monoclinic **$CuTeO_3$** material. *Phys. Rev. B* **97**, 245148 (2018).
23. Fang, C., Weng, H., Dai, X. & Fang, Z. Topological nodal line semimetals. *Chin. Phys. B* **25**, 117106 (2016).
24. Lv, B. Q. et al. Observation of three-component fermions in the topological semimetal molybdenum phosphide. *Nature* **546**, 627–631 (2017).
25. Ma, J. Z. et al. Three-component fermions with surface Fermi arcs in tungsten carbide. *Nat. Phys.* **14**, 349–354 (2018).
26. Krempaský, J. et al. Triple-point fermions in ferroelectric GeTe. *Phys. Rev. Lett.* **126**, 206403 (2021).
27. Winkler, G. W., Wu, Q., Troyer, M., Krogstrup, P. & Soluyanov, A. A. Topological phases in $InAs_{1-x}Sb_x$: from novel topological semimetal to majorana wire. *Phys. Rev. Lett.* **117**, 076403 (2016).
28. Zaheer, S. et al. Spin texture on the Fermi surface of tensile-strained HgTe. *Phys. Rev. B* **87**, 045202 (2013).
29. Xia, Y. & Li, G. Triply degenerate nodal points and topological phase transitions in $NaCu_3Te_2$. *Phys. Rev. B* **96**, 241204 (2017).
30. Song, Z.-G., Felser, C. & Sun, Y. Prediction of ideal triple degenerate points in HfIrAs and HfIrBi. *Phys. Rev. B* **98**, 165131 (2018).
31. Zhou, F. et al. Perovskite-type YRh_3B with multiple types of nodal point and nodal line states. *Phys. Rev. B* **103**, 245126 (2021).
32. Sun, Z. P. et al. Direct observation of sixfold exotic fermions in the pyrite-structured topological semimetal $PdSb_2$. *Phys. Rev. B* **101**, 155114 (2020).
33. Schröter, N. B. M. et al. Chiral topological semimetal with multifold band crossings and long Fermi arcs. *Nat. Phys.* **15**, 759–765 (2019).
34. Tang, P., Zhou, Q. & Zhang, S.-C. Multiple types of topological fermions in transition metal silicides. *Phys. Rev. Lett.* **119**, 206402 (2017).
35. Takane, D. et al. Observation of chiral fermions with a large topological charge and associated fermi-arc surface states in CoSi. *Phys. Rev. Lett.* **122**, 076402 (2019).
36. Sanchez, D. S. et al. Topological chiral crystals with helicoid-arc quantum states. *Nature* **567**, 500–505 (2019).
37. Rao, Z. et al. Observation of unconventional chiral fermions with long Fermi arcs in CoSi. *Nature* **567**, 496–499 (2019).
38. Lv, B. Q. et al. Observation of multiple types of topological fermions in PdBiSe. *Phys. Rev. B* **99**, 241104 (2019).
39. Wieder, B. J., Kim, Y., Rappe, A. M. & Kane, C. L. Double Dirac semimetals in three dimensions. *Phys. Rev. Lett.* **116**, 186402 (2016).
40. Bradlyn, B. et al. Beyond Dirac and Weyl fermions: unconventional quasiparticles in conventional crystals. *Science* **353**, aaf5037 (2016).
41. Rong, H. et al. Realization of Practical Eightfold Fermions and Fourfold van Hove Singularity in $TaCo_2Te_2$. Preprint at https://arxiv.org/abs/2208.02967 (2022).
42. Young, S. M. et al. Dirac semimetal in three dimensions. *Phys. Rev. Lett.* **108**, 140405 (2012).
43. Wang, Z. et al. Dirac semimetal and topological phase transitions in A_3Bi (A = Na, K, Rb). *Phys. Rev. B* **85**, 195320 (2012).
44. Wang, Z., Weng, H., Wu, Q., Dai, X. & Fang, Z. Three-dimensional Dirac semimetal and quantum transport in Cd_3As_2. *Phys. Rev. B* **88**, 125427 (2013).
45. Liu, Z. K. et al. Discovery of a three-dimensional topological Dirac semimetal, Na_3Bi. *Science* **343**, 864–867 (2014).
46. Neupane, M. et al. Observation of a three-dimensional topological Dirac semimetal phase in high-mobility Cd_3As_2. *Nat. Commun.* **5**, 3786 (2014).
47. Li, G., Yan, B., Wang, Z. & Held, K. Topological Dirac semimetal phase in Pd and Pt oxides. *Phys. Rev. B* **95**, 035102 (2017).
48. Gibson, Q. D. et al. Three-dimensional Dirac semimetals: design principles and predictions of new materials. *Phys. Rev. B* **91**, 205128 (2015).
49. Wu, Q., Piveteau, C., Song, Z. & Yazyev, O. V. $MgTa_2N_3$: a reference Dirac semimetal. *Phys. Rev. B* **98**, 081115 (2018).
50. Gao, Z., Hua, M., Zhang, H. & Zhang, X. Classification of stable Dirac and Weyl semimetals with reflection and rotational symmetry. *Phys. Rev. B* **93**, 205109 (2016).
51. Cao, W. et al. Dirac semimetal phase in hexagonal LiZnBi. *Phys. Rev. B* **96**, 115203 (2017).
52. Chen, C. et al. Ternary wurtzite CaAgBi materials family: a playground for essential and accidental, type-I and type-II Dirac fermions. *Phys. Rev. Mater.* **1**, 044201 (2017).
53. Xia, Y., Cai, X. & Li, G. Multitype Dirac fermions protected by orthogonal glide symmetries in a noncentrosymmetric system. *Phys. Rev. B* **102**, 041201 (2020).
54. Gao, H., Strockoz, J., Frakulla, M., Venderbos, J. W. F. & Weng, H. Non-centrosymmetric topological Dirac semimetals in three dimensions. *Phys. Rev. B* **103**, 205151 (2021).
55. Regnault, N. & Bernevig, B. A. Fractional Chern Insulator. *Phys. Rev. X* **1**, 021014 (2011).
56. Yu, R. et al. Quantized anomalous Hall effect in magnetic topological insulators. *Science* **329**, 61–64 (2010).
57. Chang, C.-Z. et al. Experimental observation of the quantum anomalous Hall effect in a magnetic topological insulator. *Science* **340**, 167–170 (2013).
58. Checkelsky, J. G. et al. Trajectory of the anomalous Hall effect towards the quantized state in a ferromagnetic topological insulator. *Nat. Phys.* **10**, 731–736 (2014).
59. Kou, X. et al. Scale-invariant quantum anomalous Hall effect in magnetic topological insulators beyond the two-dimensional limit. *Phys. Rev. Lett.* **113**, 137201 (2014).
60. Xiao, D. et al. Realization of the axion insulator state in quantum anomalous Hall sandwich heterostructures. *Phys. Rev. Lett.* **120**, 056801 (2018).
61. Aliev, Z. S. et al. Novel ternary layered manganese bismuth tellurides of the MnTe-Bi_2Te_3 system: Synthesis and crystal structure. *J. Alloy. Compd.* **789**, 443–450 (2019).
62. Sun, H. et al. Rational design principles of the quantum anomalous Hall effect in superlatticelike magnetic topological insulators. *Phys. Rev. Lett.* **123**, 096401 (2019).
63. Lee, S. H. et al. Spin scattering and noncollinear spin structure-induced intrinsic anomalous Hall effect in antiferromagnetic topological insulator $MnBi_2Te_4$. *Phys. Rev. Res.* **1**, 012011 (2019).
64. Zeugner, A. et al. Chemical aspects of the candidate antiferromagnetic topological insulator $MnBi_2Te_4$. *Chem. Mater.* **31**, 2795–2806 (2019).
65. Gong, Y. et al. Experimental realization of an intrinsic magnetic topological insulator. *Chin. Phys. Lett.* **36**, 076801 (2019).
66. Li, J. et al. Magnetically controllable topological quantum phase transitions in the antiferromagnetic topological insulator $MnBi_2Te_4$. *Phys. Rev. B* **100**, 121103 (2019).
67. Otrokov, M. M. et al. Unique thickness-dependent properties of the van der Waals interlayer antiferromagnet $MnBi_2Te_4$ films. *Phys. Rev. Lett.* **122**, 107202 (2019).
68. Deng, Y. et al. Quantum anomalous Hall effect in intrinsic magnetic topological insulator $MnBi_2Te_4$. *Science* **367**, 895–900 (2020).
69. Liu, C. et al. Robust axion insulator and Chern insulator phases in a two-dimensional antiferromagnetic topological insulator. *Nat. Mater.* **19**, 522–527 (2020).
70. Vidal, R. C. et al. Surface states and Rashba-type spin polarization in antiferromagnetic $MnBi_2Te_4$(0001). *Phys. Rev. B* **100**, 121104 (2019).
71. Ge, J. et al. High-Chern-number and high-temperature quantum Hall effect without Landau levels. *Natl Sci. Rev.* **7**, 1280–1287 (2020).
72. Chen, B. et al. Intrinsic magnetic topological insulator phases in the Sb doped MnBi2Te4 bulks and thin flakes. *Nat. Commun.* **10**, 4469 (2019).
73. Cui, J. et al. Transport properties of thin flakes of the antiferromagnetic topological insulator $MnBi_2Te_4$. *Phys. Rev. B* **99**, 155125 (2019).
74. Zhang, D. et al. Topological axion states in the magnetic insulator $MnBi_2Te_4$ with the quantized magnetoelectric effect. *Phys. Rev. Lett.* **122**, 206401 (2019).
75. Fu, L. & Kane, C. L. Topological insulators with inversion symmetry. *Phys. Rev. B* **76**, 45302 (2007).
76. Bradlyn, B. et al. Topological quantum chemistry. *Nature* **547**, 298–305 (2017).
77. Kruthoff, J., de Boer, J., van Wezel, J., Kane, C. L. & Slager, R.-J. Topological classification of crystalline insulators through band structure combinatorics. *Phys. Rev. X* **7**, 41069 (2017).
78. Po, H., Vishwanath, A. & Watanabe, H. Symmetry-based indicators of band topology in the 230 space groups. *Nat. Commun.* **8**, 50 (2017).
79. Vergniory, M. G. et al. A complete catalogue of high-quality topological materials. *Nature* **566**, 480–485 (2019).
80. Elcoro, L. et al. Magnetic topological quantum chemistry. *Nat. Commun.* **12**, 5965 (2021).
81. Gao, J., Guo, Z., Weng, H. & Wang, Z. Magnetic band representations, Fu-Kane-like symmetry indicators, and magnetic topological materials. *Phys. Rev. B* **106**, 035150 (2022).
82. Xu, Y. et al. High-throughput calculations of magnetic topological materials. *Nature* **586**, 702–707 (2020).
83. Mathew, K. et al. Atomate: a high-level interface to generate, execute, and analyze computational materials science workflows. *Comput. Mater. Sci.* **139**, 140–152 (2017).
84. Horton, M. K., Montoya, J. H., Liu, M. & Persson, K. A. High-throughput prediction of the ground-state collinear magnetic order of inorganic materials using density functional theory. *npj Comput. Mater.* **5**, 1–11 (2019).
85. Frey, N. et al. High-throughput search for magnetic and topological order in transition metal oxides. *Sci. Adv.* **6**, eabd1076 (2020).

86. Togo, A. & Tanaka, I.Spglib: a software library for crystal symmetry search. Preprint at https://arxiv.org/abs/1808.01590 (2018).
87. Gallego, S. V., Tasci, E. S., de la Flor, G., Perez-Mato, J. M. & Aroyo, M. I. Magnetic symmetry in the bilbao crystallographic server: a computer program to provide systematic absences of magnetic neutron diffraction. *J. Appl. Crystallogr.* **45**, 1236–1247 (2012).
88. Moore, G. C., Horton, M. K., Ganose, A. M., Siron, M. & Persson, K. A. High-throughput determination of Hubbard U and Hund J values for transition metal oxides via linear response formalism. Preprint at https://arxiv.org/abs/2201.04213 (2022).
89. Dascoulidou, A., Müller, P. & Bronger, W. Ternäre Mangan-Verbindungen AMnX (A = Mg, Ca, Sr oder Ba; X = Si, Ge oder Sn): Neutronenbeugungsuntersuchungen zur Charakterisierung der magnetischen Eigenschaften. *Z. Anorg. Allg. Chem.* **624**, 124–128 (1998).
90. von Schnering, H. G. et al. CsMn2P2, ein Mangan(II, III)-phosphid mit der BaZn2P2-Struktur. Mit einem Beitrag zum BaAl4-Strukturtyp. *Z. Anorg. Allg. Chem.* **628**, 2772–2777 (2002).
91. Tang, P., Zhou, Q., Xu, G. & Zhang, S.-C. Dirac fermions in an antiferromagnetic semimetal. *Nat. Phys.* **12**, 1100–1104 (2016).
92. Yang, B. J. & Nagaosa, N. Classification of stable three-dimensional Dirac semimetals with nontrivial topology. *Nat. Commun.* **5**, 4898–5898 (2014).
93. Hummel, F. Magnetism and superconductivity in layered manganese and iron pnictides. Doctoral dissertation, Ludwig-Maximilians-Universität München (2015).
94. Li, J. et al. Intrinsic magnetic topological insulators in van der Waals layered $MnBi_2Te_4$-family materials. *Sci. Adv.* **5**, eaaw5685 (2019).
95. Sun, J. et al. Accurate first-principles structures and energies of diversely bonded systems from an efficient density functional. *Nat. Chem.* **8**, 831–836 (2016).
96. Hohenberg, P. & Kohn, W. Inhomogeneous electron gas. *Phys. Rev.* **136**, B864–B871 (1964).
97. Kohn, W. & Sham, L. J. Self-consistent equations including exchange and correlation effects. *Phys. Rev.* **140**, A1133–A1138 (1965).
98. Ceperley, D. M. & Alder, B. J. Ground state of the electron gas by a stochastic method. *Phys. Rev. Lett.* **45**, 566–569 (1980).
99. Perdew, J. P. & Zunger, A. Self-interaction correction to density-functional approximations for many-electron systems. *Phys. Rev. B* **23**, 5048–5079 (1981).
100. Perdew, J. P., Burke, K. & Ernzerhof, M. Generalized gradient approximation made simple. *Phys. Rev. Lett.* **77**, 3865–3868 (1996).
101. Kresse, G. & Joubert, D. From ultrasoft pseudopotentials to the projector augmented-wave method. *Phys. Rev. B* **59**, 1758–1775 (1999).
102. Kresse, G. & Hafner, J. Ab initio molecular dynamics for liquid metals. *Phys. Rev. B* **47**, 558–561 (1993).
103. Kresse, G. & Furthmüller, J. Efficient iterative schemes for ab initio total-energy calculations using a plane-wave basis set. *Phys. Rev. B* **54**, 11169–11186 (1996).
104. Sancho, M. P. L., Sancho, J. M. L., Sancho, J. M. L. & Rubio, J. Highly convergent schemes for the calculation of bulk and surface Green functions. *J. Phys. F. Met. Phys.* **15**, 851–858 (1985).
105. Marzari, N. & Vanderbilt, D. Maximally localized generalized Wannier functions for composite energy bands. *Phys. Rev. B* **56**, 12847–12865 (1997).
106. Mostofi, A. A. et al. wannier90: a tool for obtaining maximally-localised Wannier functions. *Comput. Phys. Commun.* **178**, 685–699 (2008).
107. Wu, Q., Zhang, S., Song, H.-F., Troyer, M. & Soluyanov, A. A. Wanniertools : an open-source software package for novel topological materials. *Comput. Phys. Commun.* **224**, 405–416 (2018).

ACKNOWLEDGEMENTS

This work is supported by the Shanghai Technology Innovation Action Plan 2020-Integrated Circuit Technology Support Program (Project No. 20DZ1100605), the National Natural Science Foundation of China under Grant No. 11874263, Sino-German mobility program (M-0006), the National Key R&D Program of China (2017YFE0131300). W.S. wants to thank the financial support of the Science and Technology Commission of Shanghai Municipality (STCSM) (Grant No. 22ZR1441800), Shanghai-XFEL Beamline Project (SBP) (3101150550585892016 1A2101001). Part of the calculations was performed at the HPC Platform of ShanghaiTech University Library and Information Services, the School of Physical Science and Technology, and the Scientific Data Analysis Platform of Center for Transformative Science.

AUTHOR CONTRIBUTIONS

G.L. conceived and designed the project. Y.S. and G.L. performed all the calculations with the help of J.H., X.C., W.S., and Y.X. X.X. and Y.C. contributed to the scientific discussion. The manuscript was written by Y.S. and G.L. with contributions from all authors.

COMPETING INTERESTS

The authors declare no competing interests.

ADDITIONAL INFORMATION

Supplementary information The online version contains supplementary material available at https://doi.org/10.1038/s41524-022-00954-w.

Correspondence and requests for materials should be addressed to Gang Li.

Reprints and permission information is available at http://www.nature.com/reprints

Publisher's note Springer Nature remains neutral with regard to jurisdictional claims in published maps and institutional affiliations.